

PAPER • OPEN ACCESS

Possible charge ordering and anomalous transport in graphene/graphene quantum dot heterostructure









To cite this article: Rajarshi Roy *et al* 2024 *J. Phys.: Condens. Matter* **36** 265601

View the [article online](#) for updates and enhancements.

You may also like

- [Adhesion and migration of CHO cells on micropatterned single layer graphene](#)
S Keshavan, R Oropesa-Nuñez, A Diaspro et al.
- [Hybrid graphene-manganite thin film structure for magnetoresistive sensor application](#)
Rasuole Lukose, Nerija Zurauskiene, Saulius Balevicius et al.
- [Tunable Schottky contact at the graphene/Janus SMO₂SiN₂ interface for high-efficiency electronic devices](#)
Son-Tung Nguyen, Cuong Q Nguyen, Yee Sin Ang et al.

Possible charge ordering and anomalous transport in graphene/graphene quantum dot heterostructure

Rajarshi Roy^{1,9,*} , David Holec^{2,*} , Lukáš Michal¹, Dušan Hemzal³ , Saikat Sarkar⁴, Gundam Sandeep Kumar⁵ , David Nečas⁶ , Meena Dhankhar⁷ , Preeti Kaushik³, I Jénnifer Gómez^{3,8}  and Lenka Zajíčková^{3,6} 

¹ Central European Institute of Technology, Masaryk University, Kamenice 5, 62500 Brno, Czech Republic

² Department of Materials Science, Montanuniversität Leoben, Franz-Josef-Strasse 18, A-8700 Leoben, Austria

³ Department of Condensed Matter Physics, Masaryk University, Kotlářská, 611 37 Brno, Czech Republic

⁴ Thin Film and Nanoscience Lab, Department of Physics, Jadavpur University, Kolkata 700032, India

⁵ Department of Chemistry, KU Leuven, Celestijnenlaan 200 F, 3001 Heverlee, Belgium

⁶ Central European Institute of Technology, Brno University of Technology, Purkyňova 123, 612 00 Brno, Czech Republic

⁷ National Centre for Nano Fabrication and Characterization, Oersteds Plads—Building 347, Kongens Lyngby 2800 DK, Denmark

⁸ Centro Interdisciplinar de Química e Biología (CICA), Universidade da Coruña, Rúa as Carballeiras, 15071 A Coruña, Spain

E-mail: rajarshiroy84@gmail.com and david.holec@unileoben.ac.at

Received 17 November 2023, revised 14 February 2024

Accepted for publication 8 March 2024

Published 2 April 2024



CrossMark

Abstract

Observations of superconductivity and charge density waves (CDW) in graphene have been elusive thus far due to weak electron–phonon coupling (EPC) interactions. Here, we report a unique observation of anomalous transport and multiple charge ordering phases at high temperatures ($T_1 \sim 213$ K, $T_2 \sim 325$ K) in a 0D–2D van der Waals (vdW) heterostructure comprising of single layer graphene (SLG) and functionalized (amine) graphene quantum dots (GQD). The presence of functionalized GQD contributed to charge transfer with shifting of the Dirac point ~ 0.05 eV above the Fermi level (*ab initio* simulations) and carrier density $n \sim -0.3 \times 10^{12} \text{ cm}^{-2}$ confirming p-doping in SLG and two-fold increase in EPC interaction was achieved. Moreover, we elucidate the interplay between electron–electron and electron–phonon interactions to substantiate high temperature EPC driven charge ordering in the heterostructure through analyses of magnetotransport and weak anti-localization (WAL)

⁹ Present address: Institute of Physics of the Czech Academy of Sciences, Cukrvarnicka 10/112, Prague 16200, Czech Republic

* Authors to whom any correspondence should be addressed.



Original Content from this work may be used under the terms of the [Creative Commons Attribution 4.0 licence](https://creativecommons.org/licenses/by/4.0/). Any further distribution of this work must maintain attribution to the author(s) and the title of the work, journal citation and DOI.

framework. Our results provide impetus to investigate strongly correlated phenomena such as CDW and superconducting phase transitions in novel graphene based heterostructures.

Supplementary material for this article is available [online](#)

Keywords: graphene, graphene quantum dots, heterostructure, charge ordering, Raman spectroscopy, low temperature transport, *ab initio* simulation

1. Introduction

Emergence of charge ordering and charge density wave (CDW) phase transitions in intercalated and bilayer graphene-based systems have generated a great deal of interest in recent years due to their fundamental importance [1–3]. Graphene presents a remarkable opportunity to investigate such CDW phase transitions in low-dimensional carbon materials thanks to its unique Dirac-like linear band dispersion. Essentially, CDW can be characterized as a sudden appearance of a periodic modulation in electron density accompanied by lattice distortions in low-dimensional materials [1, 2]. In layered materials such as transition metal dichalcogenides (TMDC) and high temperature cuprate superconductors, both CDWs and superconductivity were reported to appear as a consequence of reducing symmetry to reach the ground state [4–6]. Hence, discerning the intimate connection between the competing superconductivity and CDW phases is a fascinating problem in this domain. In graphene, a CDW is closely related to the doping or intercalation primarily attributed to its Dirac-like band dispersion at the K -point in the first Brillouin zone (BZ), giving rise to a special Van Hove Singularity (VHS), resulting in a kink in the density of states (DOS) at the Fermi level [2, 3, 7]. The fundamental idea is to enhance the much weaker electron–phonon coupling (EPC) in graphene, through intercalation or doping, enough to observe such CDW instabilities at very low energies [8, 9]. Recently, it was shown that the creation of a Moiré pattern between two graphene sheets generates a magic-angle superlattice and forms a flat band with bandwidth on the order of 10 meV whose carrier density can be tuned by electrical gating to show superconductivity [10]. Hence, formation of such a flat band at very low energies through structural modifications and doping in graphene can be crucial for observation of CDW and superconducting phase transitions as well. Moreover, van der Waals (vdW) heterostructures fabricated with graphene and other two-dimensional (2D) materials (e.g. h-BN, MoS₂, WS₂) were found to have properties such as high carrier mobility electronic transport, valleytronics and ultrafast charge transfer carrier dynamics [11–13]. In recent years, novel vdW heterostructures with quantum dots on graphene and other 2D materials (MoS₂) have demonstrated charge transfer properties [14]. N-doping in MoS₂ was shown due to addition of the functional GQDs [15] while electrical polarization induced ultrahigh responsivity photodetectors based on graphene and graphene quantum dot have been reported as a result of efficient interfacial charge transfer process between the two materials [16]. Hence it is expected that a combination of graphene with GQD

could potentially enhance the EPC for observation of novel temperature dependent phase transitions including CDW and superconductivity. Here, we report on such a 0D–2D vdW heterostructure comprising of a single layer graphene (SLG) and functional (amine) GQD showing anomalous transport behavior and possible charge ordered phase transitions at high temperatures. Furthermore, using *ab initio* simulations, low temperature Raman spectroscopy and electrical transport, we elucidate the mechanism that is intricately tied to interfacial charge transfer and doping, EPC, electron scattering, thermal and anharmonic effects within the two interacting materials.

2. Methods

2.1. Sample preparation

Commercially available easy transfer single layer graphene sample from Graphenea was purchased, was transferred on to Si/SiO₂ substrates with thickness 285 nm using wet transfer method following their standard prescribed protocol [17]. To prepare the amine functional graphene quantum dots, at first graphene oxide sheets (GOS) were prepared using modified Hummer’s method from finely coarse graphite powder. Then, 5 ml of GOS solution (1 mg ml⁻¹ loading), 5 ml of de-ionized water and 3 ml of ammonia solution was added together and mixed in a beaker with constant stirring for 30 min. This resultant solution was transferred to a Teflon-lined autoclave and put in a hot oven 150 °C for 5 h in order to carry out a hydrothermal reaction. After the completion of the reaction, the autoclave was taken out of the oven and kept aside to bring down the solution to room temperature. Afterwards the large fragments of the quantum dots were removed by filtering using a 0.22 μm anopore inorganic membrane (Anodisc TM, Whatman). Furthermore, the filtered solution was heated up to ~ at 80 °C for 1 h to remove the excess ammonia content. Finally, ultrafiltration was carried out using a centrifugal filter device with a 10 kDa molecular weight cut-off membrane (Sartorius) to filter out the unwanted small fragments and achieve a uniform size distribution of the functional quantum dots [18, 19]. Finally, the composite heterostructure, graphene-GQD (H) sample was prepared by thinly spin-coating the functional GQD on top of pre-transferred single graphene over 285 nm Si/SiO₂ for Raman measurements. The spin coating was carried out for 1 min with 1000 r.p.m followed by 1500 r.p.m. The loading concentration of the GQD was 1 mg ml⁻¹.

The electrodes were then lithographically prepared on the silicon substrate with 285 nm SiO₂ by lift-off technique. The

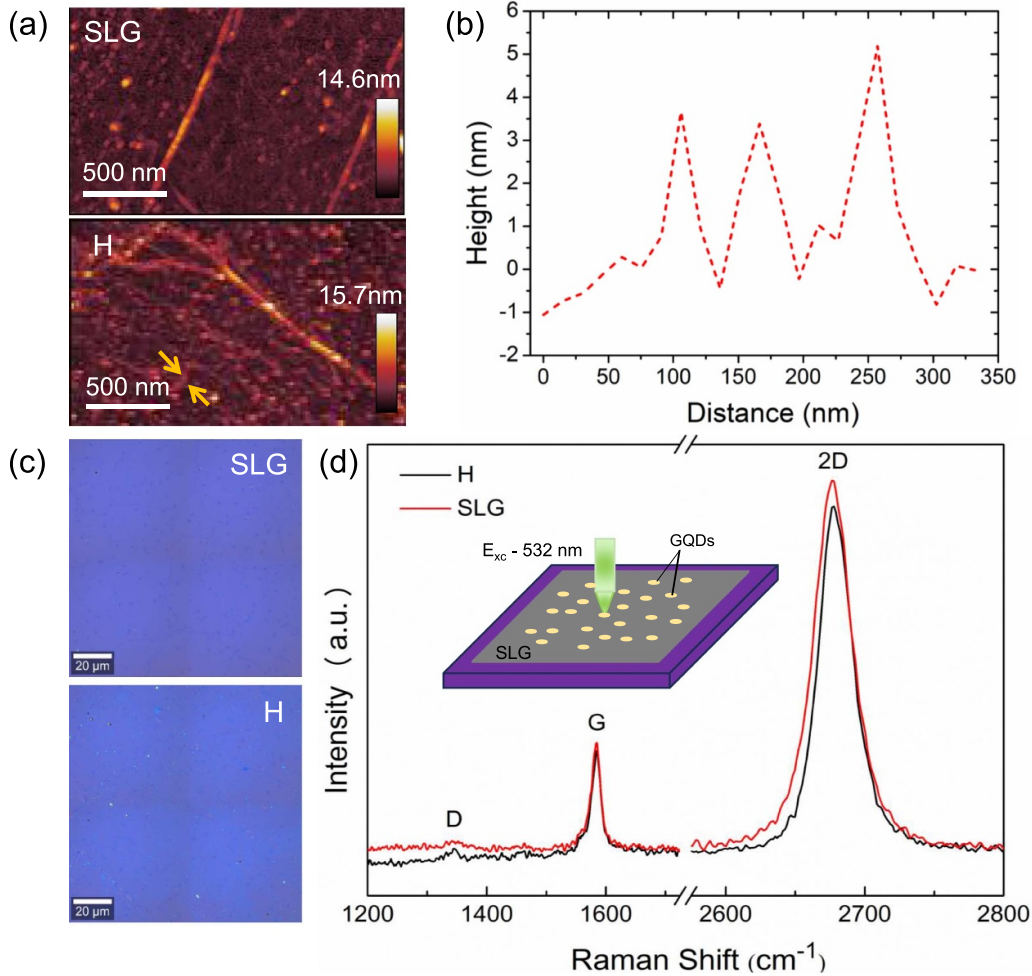


Figure 1. General features of the prepared samples. (a) Atomic force microscopy (AFM) image of the SLG and the heterostructure (H) sample. (b) The height profile with the height profile corresponding to the orange arrowheads (guide to the eye) where the GQDs are top of graphene. (c) Optical images of SLG and the H samples, respectively. (d) Raman spectra of SLG and the H sample at room temperature. Inset: Schematic representation of the graphene-GQD heterostructure (H) sample on Si/SiO₂ substrate.

graphene sample was then preheated/prebaked on a hotplate at 180 °C for 15–20 min to remove the humidity from the sample. A resist film of poly-methyl methacrylate (PMMA) 950k (allresist AR-P 679.04) resist at 2000 r.p.m for 1 min results in film thickness of approximately 350 nm. The sample was then soft baked at 180 °C for 3 min to harden the PMMA layer. The electrodes were then exposed by electron beam lithography machine RAITH 150Two, with a dose factor of 250 $\mu\text{C cm}^{-2}$ at 20 keV, followed by chemical development in MIBK based developer (allresist AR 600-56) for 1 min and then evaporation of Ti/Au (5/100 nm) layer in BESTEC evaporator. The sample was then put in acetone for 1 h, later the excess metal was removed by spraying acetone over the sample. For the heterostructure device, afterwards the GQD (1mg ml⁻¹) was put on top of graphene. The fabricated interelectrode distance was kept at 5 μm .

2.2. Characterizations

The surface topography of all the samples was estimated using Atomic Force Microscopy (AFM, Bruker Dimension

ICON) using the tapping mode configuration. The density of the functional GQD on graphene was calculated from the AFM image (figure 1(a)) of the H sample using open-source scanning probe microscopy software Gwyddion [20]. The as-synthesized GQDs have been characterized for structural, compositional, and optical analysis. High Resolution Transmission Electron Microscopy (HRTEM) analysis was carried out (JEOL-JEM 2010, 200 kV) to determine the structural characteristics such as the size distribution, morphology and for high resolution lattice imaging of the material. Fourier transform infrared (FTIR) spectroscopy was carried out on the GQD sample using a Shimadzu-IR (Prestige-21) spectrometer to determine the existence of amine bonding and the different functional groups present in the quantum dots. UV-Vis (Shimadzu UV 1700 spectrophotometer) characterizations were conducted to observe the optical absorption edge in the functional GQDs, and the excitation dependent Photoluminescence (Horiba Jobin Yvon Fluoromax-4) was measured with a Xenon lamp source fitted with a monochromator. The low temperature Raman measurements were conducted using in Via confocal micro-Raman spectrometer

(Renishaw) and 532 nm excitation by MX532 DPSS laser (Coherent) with nominal rating 10 mW. The power of the laser was tuned down using ND filters to a constant 10% of the nominal power of the laser source and focused on to sample using 10x LWD objective (Mitutoyo) with numerical aperture (NA) 0.28. The samples were placed in ST-100-FTIR cryostat (Janis Research) evacuated to HV using TSH 064D turbo-molecular pump (Pfeiffer vacuum) and cooled down to LN2 temperature. All spectra for the samples were collected from 78–295 K by cooling down the sample to liquid nitrogen temperature and then measured on the heating cycle till room temperature using optical grating 1800 grooves mm^{-1} . To fit the temperature dependent G band and the 2D band peaks in SLG and the heterostructure, we mainly used two distinct techniques comprising of purely Lorentzian and mixed convolution of Gaussian and Lorentzian (GL) of both peaks were used [21]. We found that GL (100) for the G band peak and (GL (80) for the 2D peak gave the best result in terms of fitting accuracy and reduced χ^2 value in both samples after linear background correction. All resistance-temperature (RT) measurements were carried out using 4-probe attachment in VERSALAB by Quantum Design under both heating and cooling cycles from 50 to 400 K. For the magnetoresistance measurements, an out-of-plane magnetic field (± 3 T) was applied during measurement at specific temperatures.

2.3. *Ab initio* simulations

The model was firstly fully structurally relaxed using Vienna *Ab initio* Simulation Package (VASP) [22–24] employing projector-augmented wave enabled pseudopotentials [24]. The initial relaxations were performed using a single k -point (Γ) sampling the reciprocal space (hence allowing using the more efficient gamma-version of VASP), while the final relaxation step and electronic structure data were calculated with Γ -centered $4 \times 4 \times 1$ k -mesh. We used plane-wave cut-off energy of 400 eV, and convergence criteria of 10^{-6} eV and 10^{-3} eV (per simulation box with 576 atoms) for electronic and ionic loops, respectively. During the structural relaxation, all atoms of the functionalized QD were allowed to move, whereas graphene substrate was fixed flat. The density of electronic states was calculated with an energy resolution of 0.026 eV. The bandstructure was unfolded using the BandUP code [25, 26], and only points with weights $\delta N > 0.05$ were plotted for clarity. The model, as well as the charge density and electron localization function, were visualized using the VESTA3 software [27]. Parts of the pymatgen Python library were used for data processing [28].

3. Results and discussion

3.1. Sample features

In figure 1(a), depicts atomic force microscopy (AFM) image of the SLG and uniform graphene-GQD heterostructure (H) film together with a height profile (figure 1(b)) along the line in between the orange arrowheads (guide to the eye in figure 1(a)). It suggests that when the GQDs lie on top of

graphene, account for maximum upto ~ 3 layers in thickness [29] the optical images from SLG and the H sample along with their Raman spectra at room temperature. Unlike SLG, the H sample contains faint tiny whitish spots distributed throughout (over SLG) due to presence of the GQDs. Both samples show mainly the characteristics of the SLG in the Raman spectra with G band position at 1585 cm^{-1} and the I_{2D}/I_G ratio ~ 3 . However, we observe slight blue shift of the 2D band position ($\sim 2678 \text{ cm}^{-1}$) and change in phonon linewidth for the H sample in comparison to that of SLG ($\sim 2676 \text{ cm}^{-1}$). This is a clear indication of charge transfer in graphene caused by the interaction with functionalized GQDs [30]. Moreover, we observe a slight increase in the D band in the H sample which indicates the out-of-plane heterostacking of functionalized GQD over SLG.

3.2. Low-temperature Raman spectroscopy

Raman spectroscopy is an important graphene characterization technique, allowing the estimation of the number of layers, defects, doping, stacking order and a breakdown of the adiabatic Born–Oppenheimer (BO) approximation by critically analyzing the distinctive, D, G and 2D (double resonance) bands and their overtones [31]. Taking it a step further, Calizo *et al* [32] determined the temperature coefficient of thermal expansion in SLG on 285 nm Si/SiO₂ substrate using a non-invasive Raman-based optothermal technique. For graphene, the G band dispersion (ω_G, Γ_G), is the most crucial as it is known to be highly temperature sensitive and originates from the in-plane E_{2g} phonon mode at the center of BZ (Γ_G) [33]. Hence, the temperature dependence of both positions together with the full width at half maxima (ω_G, Γ_G) of the G band are crucial for determining the temperature coefficient for thermal expansion, thermal conductivity, phonon lifetime and anharmonic contributions in graphene [32–34].

Figure 2 represents the temperature dependent dispersion relationships resulting from the fitting of the G and the 2D bands (78–295 K) in Raman spectra. In figure 2(a), it is observable that ω_G is red shifted with considerable broadening of Γ_G and increases more slowly for H in comparison to SLG at lower temperatures. We propose that there is a transition region between ~ 175 – 220 K below which the ω_G slope becomes distinctly different from that of the SLG, and which corresponds to where also the onset of the Γ_G broadening appears. Above this temperature, the Raman signal of SLG and H samples are almost identical. Normally, such behavior of the ω_G slope and broadened Γ_G are indicators of (1) temperature-dependent phase transition and/or (2) anharmonic contributions. The temperature dependence of ω_G in graphene can be represented by $\omega = \omega_0 + \chi T$, where ω_0 is the G band frequency when the temperature is extrapolated to 0 K and χ is the first order temperature coefficient evaluated to be $-0.016 \text{ cm}^{-1} \text{ K}^{-1}$ for SLG by Calizo *et al* [32]. However, other values were reported, depending on the quality, substrate, and synthesis conditions of the SLG. We evaluate the temperature coefficient $\sim -0.03 \text{ cm}^{-1} \text{ K}^{-1}$ in our SLG from the linear fitting of the slope ($R^2 \sim 0.9$) over the whole range that matches well the previous result reported by Nyugen *et al* [35]. For the heterostructure, the

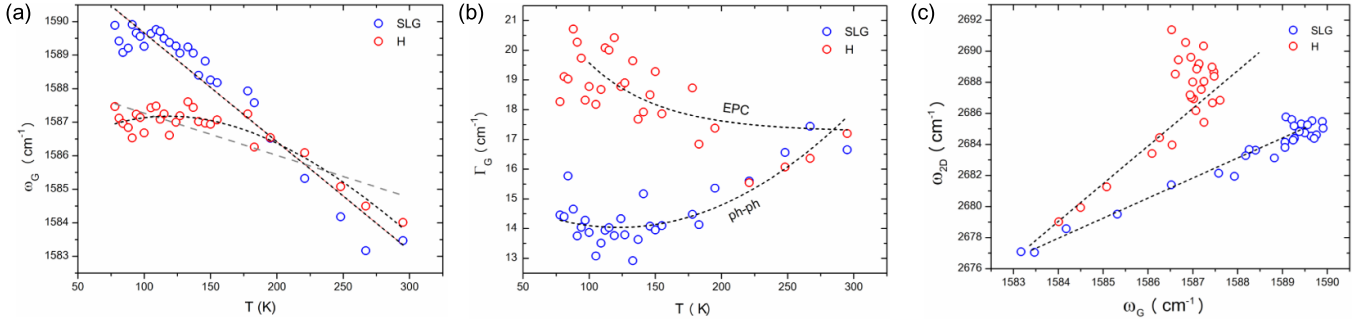


Figure 2. Low temperature Raman spectroscopy. (a) Temperature dependence of the G-band peak frequency (ω_G) for SLG and H sample. The red and the dotted grey colored lines show the linear fit to extract the negative temperature coefficient in SLG and H, respectively. The black dotted line represents the non-linear polynomial function fit for the H sample. (b) Temperature dependence of the corresponding full width half maxima (Γ_G) for SLG and H sample. The black dotted lines here represent the fitting to extract both $\gamma_{ph-ph}(0)$, $\gamma_{e-ph}(0)$ for the respective samples to validate the almost two-fold enhancement of EPC in the heterostructure from the fitting procedure described in [34, 36]. (c) Correlation plot between the position peak frequency dependence of G-band (ω_G) against 2D band (ω_{2D}) for SLG and H sample. The dotted lines represent the linear fitting for the respective samples.

linear fit gave the value $\sim -0.012 \text{ cm}^{-1} \text{ K}^{-1}$. This renormalization of temperature coefficient itself can play an important role for determining the thermal conductivity for such graphene-graphene quantum dot based heterogeneous interfaces. However, we find that there is substantial effect of anharmonicity that reflects in the distinct modification of the slope in the heterostructure. Cong and Yu [34] showed a polynomial fitting approach to fit the position dependence of the weak low frequency C-mode shear phonons in folded graphene to effectively demonstrate the anharmonicity. Hence, refitting of the temperature dependent ω_G dispersion for the heterostructure with a non-linear polynomial function yields a much better fit than linear model in this case. Moreover, the anharmonic processes can give rise to EPC in the heterostructure in comparison to SLG. To be more specific about the extent of the coupling, we fit the temperature dependent Γ_G dispersion as described in previous reports [34, 36] and estimate nearly two-fold enhancement in the EPC contribution of the heterostructure, which is absent for SLG. Hence, we attribute the temperature dependent broadening of Γ_G to be a sign of phonon softening in the heterostructure due to enhanced EPC. The details of the fitting are provided in the supplementary material. Such an increase in EPC is also reported for a similar system in magic angle bilayer graphene [37]. In figure 2(c), we show the ω_G vs ω_{2D} dispersion for SLG and H. From this relationship, one can discern the effects of doping and/or stress-strain by computing the slope for the individual samples. Generally, a negative slope value ~ -0.2 implies n-type charge carriers in SLG, whereas a positive slope value $\sim 0.6-0.7$ can be attributed to p-type carriers [38]. Larger positive values ~ 0.7 , are considered a manifestation of predominant p-type carriers with added contribution of stress-strain dependent effects within the system [30]. In our samples, we find a slope of ~ 1.2 for SLG, while in the heterostructure, it increases to 2.8. Therefore, in both our samples, p-type charge carriers dominate, with the H sample exhibiting a more pronounced effect of the stress-strain component overall. The effects of strain in the 2D materials can lead to exotic charge ordering driven phase transitions [39].

Our Raman spectroscopic investigations clearly point to enhanced EPC and increased carrier density in graphene interacting with the GQDs. Hofmann *et al* [40] recently reported on CDW in a graphene-TCNQ framework. CDW was achieved by careful tuning of the dielectric function ϵ of the system determining the effective Coulombic interaction in graphene defined by the ratio of E_C/E_K of the pairwise Coulombic repulsion E_C and the particles kinetic energy E_K . It is found that adsorption of TCNQ in the low-density regime is able to generate enough carriers to modulate the screening of the dielectric function triggering CDW which cannot be achieved by conventional doping or intercalating dopants. We achieve a similar low carrier density for the H sample after addition of functionalized GQDs in graphene [41]. Hence, to combine EPC interaction with the Coulombic interaction, one can draw reference from the generalized Hubbard-Holstein model. Here, an additional EPC interaction term is added with the existing onsite Coulomb repulsion (U) and the long-range coulomb interaction (V) terms within the existing Hubbard Hamiltonian [42]. Hence, the presence of both Coulomb interactions and EPC can contribute to CDW, or charge ordered phase transitions in the heterostructure which we discuss below from the point of view of electrical transport.

3.3. Low-temperature electrical transport

In figure 3, we show the detailed electrical transport measurements of our samples. The four-terminal resistance-temperature (R - T) profile measurements were carried out in both the heating and the cooling cycle for SLG and the H sample as shown in figure 3(a). For SLG the R - T behavior corresponds to a semi-metal with very low resistance span ranging from 0.64Ω at 50 K to 1.36Ω at 400 K in the heating cycle. However, there is no observable change in the R - T profile in both heating and cooling cycles. In contrast, the H sample showed an anomalous ‘bow-tie’ or ‘butterfly’ loop in the cooling-heating R - T sequence with a higher average resistance profile (4–6 times) as compared to SLG. Analyzing the heating cycle for the H sample, we observe that the R - T

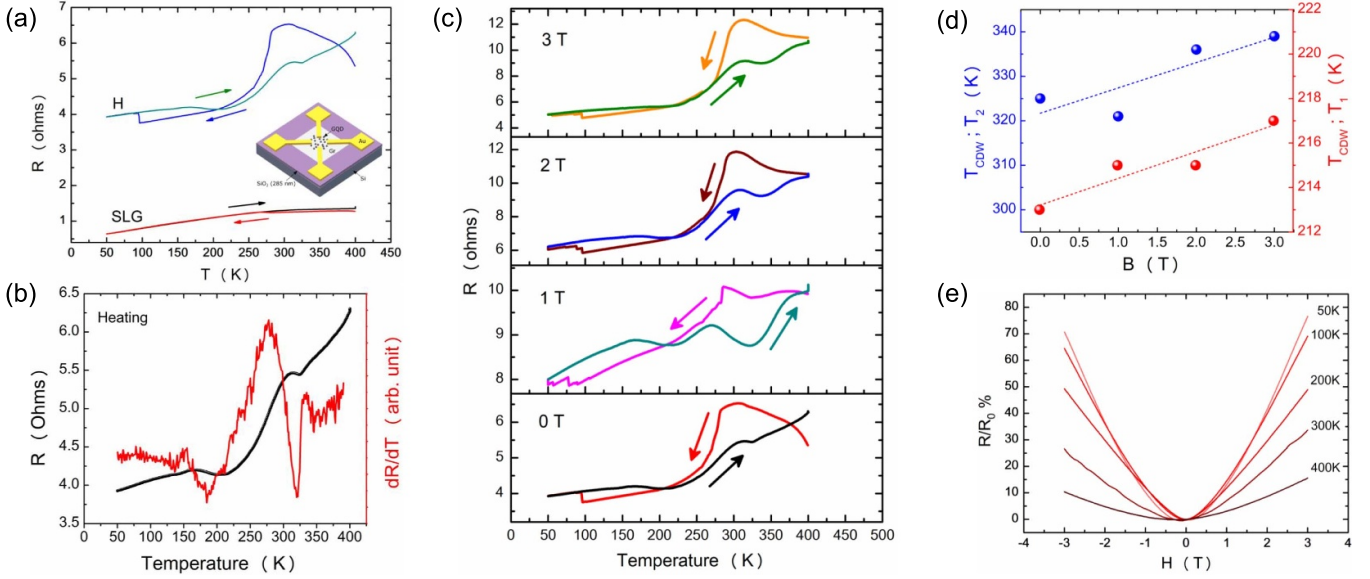


Figure 3. Low temperature electrical transport measurement. (a) Resistance as a function of temperature for SLG and H. The red and the black line represent the data for SLG in cooling and heating cycle respectively while the blue and green represent the same for sample H. Inset: Schematic representation of the device measured for the heterostructure. (b) Resistance—temperature profile of the H sample during the heating cycle plotted alongside dR/dT as a function of temperature showing two derivative minima (c) Temperature dependent evolution of the resistance profile for the H sample under different out-of-plane applied magnetic field during the heating and cooling cycle. (d) Variation of the CDW transition temperatures (T_{CDW}) corresponding to T_1 and T_2 transition points under the increasing applied magnetic field. (e) Magnetoresistance of the H sample at different temperatures from 50 to 400 K.

profile has a prominent s-shaped bend between 150–300 K. In addition, there are abrupt changes in resistance at certain temperatures usually associated with CDW-like phase transitions [43] as a manifestation of charge ordering. The presence of prominent closed loops between heating and cooling cycles in the R - T profile have been previously suggested to indicate a possible first order CDW like phase transition with opening of a ‘pseudogap’ at the K -point near the Fermi level, originating from the Fermi surface nesting due to an enhanced EPC [43–45]. We observe a distinctly sharp step-like modulation of the resistance to close the loop ~ 95 K in the cooling cycle. A similar feature has been previously observed in a layered quasi two-dimensional chalcogenide $1T$ - TaS_2 crystal, which exhibits multiple competing ground states under equilibrium conditions, whereas an incommensurate CDW phase is associated with a lattice distortion. Furthermore, upon cooling, the modulations sharpen to form star shaped polaron clusters whose ordering can cause multiple temperature dependent phase transitions from nearly commensurate to gapped commensurate phases [46, 47]. In figure 3(b), we plot the temperature dependence of differential resistance (figure 3(b)) of the H sample in heating cycle, which depicts two derivative minima, at two distinct temperatures. Furthermore, we identify the phase transition T_{CDW} temperature from the kink points in the R - T profile, one at the temperature 213 K (T_1) and the other near to the room temperature 325 K (T_2). This signifies the existence of multiple charge ordering phases in two distinct regions, a smaller closed loop from 50 to 220 K followed by the bigger from 220 to 400 K completing the ‘bowtie’ R - T heating and cooling sequence in the heterostructure. There are several recent observations of multistage charge

ordering and CDW phase transitions that is well reported among the material class of transition metal dichalcogenides [46–51]. Recent report also indicates a new type of anomalous charge density wave and its suppression in $NbSe_2$ /graphene heterostructure [52].

Furthermore, we explored the magnetic field dependence on the R - T profile on the heterostructure sample (figures 3(c) and 1(d)). The nature of the ‘butterfly’ R - T loops also remains unchanged under the applied magnetic field. However, by applying a perpendicular-to-sample increasing magnetic field (1–3 T), there is increase in both phase transition temperatures (T_1, T_2). Previously, shifting of CDW transition temperature has been observed in temperature dependent transport measurements of Kish graphite samples under high magnetic fields which originate from the large effective masses of the carriers along ordered c -axis orientation [53]. However, in our system the thickness is only approximate as a quasi-2D system unlike in the case of bulk graphite and measured at considerably lower magnetic field. Therefore, the origin of the transition temperature shift with magnetic field remains unclear in this scenario. In figure 3(e), the R/R_0 magnetoresistance (MR) profiles for different temperatures are shown for the H sample. We find the MR from 10% at 400 K increases to almost 70%–75% at 50 K while having a parabolic H^2 non-linear dependence on the magnetic field (figure S6) within the measured temperature range. According to Ke *et al* [54] such large positive MR can arise due to partially gapped Fermi surfaces resulting from the density waves.

Controversy related to the origin of charge ordering in quasi 2D materials has been well known in recent years. For example, in $2H$ - $NbSe_2$, evidence of Fermi surface nesting of

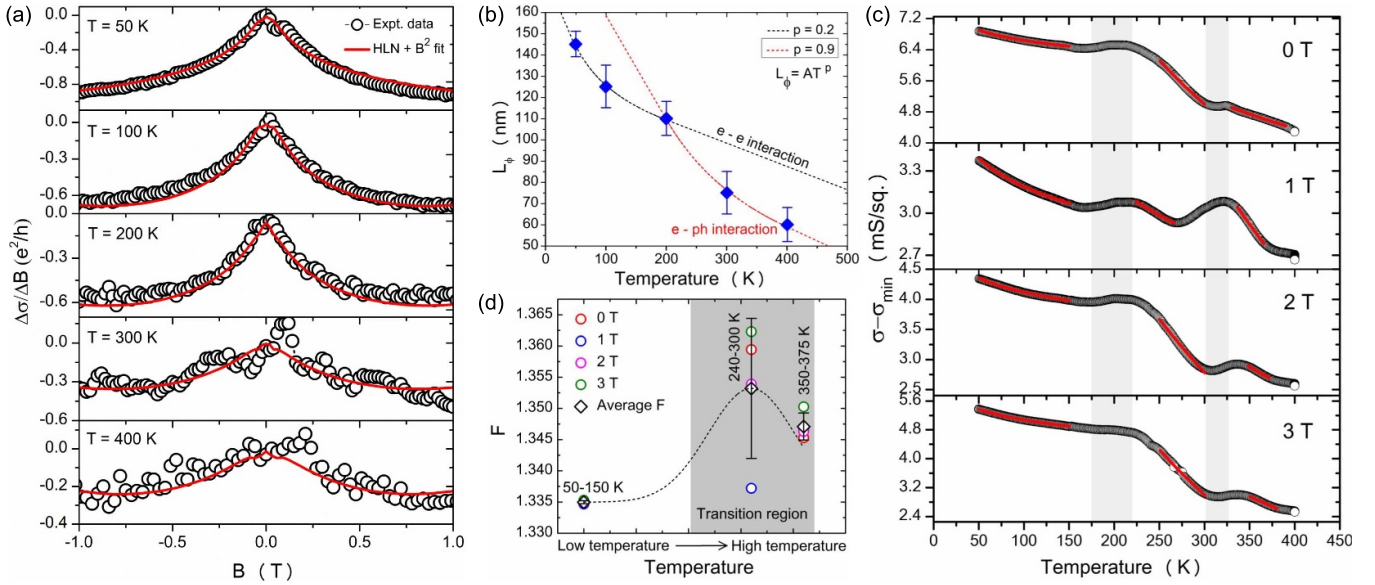


Figure 4. Correlation between EPC and EEI interactions from magnetotransport. (a) Fitting of normalized magnetoconductance using the modified HLN + B^2 fitting equation as shown in [61] from 50 K, 100 K to 400 K. (b) Temperature dependence of the coherence length and extraction of the exponent p using the relation $L_\phi = AT^p$. (c) Fitting of the differential conductivity vs temperature with equation given in [63], at different applied perpendicular magnetic from 1–3 T at three distinct temperature regions i.e., low, mid and high near the charge ordering transitions. (d) Temperature dependence of the screening factor (F) at different magnetic fields extracted using the equations in [63].

the CDW phonon wavevector is not found from the angle-resolved photoelectron spectroscopy (ARPES). Hence, an unconventional second order phase transition is more plausible related to \vec{q} dependent EPC [55]. Moreover, CDW in topological insulator (TI) Bi_2Se_3 [56], has shown that both the first order and the second order phase transitions can be possible in the same material. It is known that, strong electron–electron interactions (EEI) can trigger multiple charge ordering states as well [57–59]. Anomalous resistivity fluctuations due to weak localization (WL) in disorderly magnetic topological insulators have been also reported [60].

To shed more light on our case, we employ the weak localization (WL) model and implement the fitting of the magnetoconductance (MC) correction using a modified expression of the famed Hakami Larkin Nagaoka (HLN) equation as shown in figure 4(a) [61]. In this modified expression, there is a correction factor βB^2 which is added to the original expression where β is a constant. Therefore, using this framework, we extract the coherence length (L_ϕ) which is essential to analyze the EEI interactions and the extent of the electron dephasing mechanism in a phase coherent system. As shown in figure 4(b), we find that the extracted L_ϕ , from the fit is decreasing with increasing temperature, with the pre-factor $\alpha = 1$ corresponding to weak-anti localization. Furthermore, we fit the two slopes of the temperature dependent L_ϕ with the power law equation with the value of exponent determining the contribution of the EEI or EPC interactions. From the literature it is well known that L_ϕ decays with temperature dependent exponent ~ 0.75 considering EPC interaction. It is ~ 0.50 for EEI in the 2D limit and ~ 0.33 for 1D scenario. For variable range hopping mechanism, the exponent is estimated to be ~ 0.25 for 3D systems [61]. In our case, using

the equation $L_\phi = AT^p$ [62], we find the exponent p in the high temperature regime to be ~ 0.8 , thus matching closely for EPC scenario, and ~ 0.27 at low temperatures corresponding to the EEI mechanism. This indicates that at high temperatures, the charge ordering is taking place is mainly influenced by EPC.

Henceforth, the temperature dependent Coulomb screening term F is determined using the equation for the temperature dependent corrected conductance for 2D system corresponding to the heterostructure [63]. Figure 4(c) depicts the stacked fitting representation of the temperature dependent corrected conductivity profile in the heating cycle at different temperature regions (low: 50–150 K, mid: 240–300 K, high: 350–375 K) under 1–3 T applied magnetic field. The details of the calculations are provided in the supplementary information. We find high screening factor to be $F \gg 1$ throughout the temperature range, thus implying presence of strong electron–electron correlations in the H sample [64]. As the magnetic field is increased (1–3 T) F increases up to 1.35–1.34 for both 240–300 K and 350–375 K regions. The formation of anomalous hidden concomitant ‘Mott insulating’ phases in our doped low bandgap heterostructures could be possible analogous to TaS_2 [47]. Recently, Gauzzi *et al* suggested competing EPC and EEI interactions triggering charge ordering in TiSe_2 is possible [58].

3.4. *Ab initio* simulations

In figure 5, we introduce a model of our 0D-2D heterostructure (H) consisting of SLG and the GQD functionalized with amine groups. Figure 5(a) shows the top view of the relaxed heterostructure with the functional GQD with a radius $R \sim 5 \text{ \AA}$,

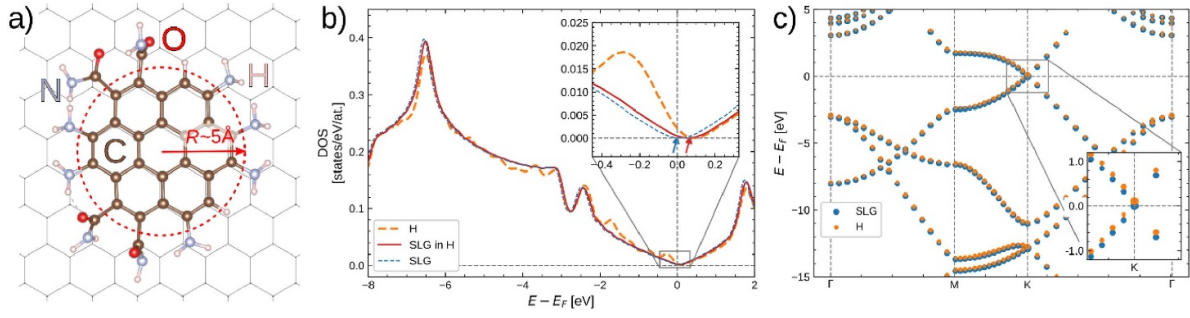


Figure 5. Theoretical simulation of the 0D–2D heterostructure. (a) Top view of the optimized supercell of the vdW stacked functional GQD–SLG heterostructure (H) configuration with the radius of the GQD $R \sim 5 \text{ \AA}$. (b) Combined total density of states (TDOS) of the heterostructure (H), single layer graphene (SLG) and the SLG isolated from the H configuration. Inset: Zoomed in perspective of the combined TDOS in all the three configurations close to the Dirac point. (c) Superimposed combined bandstructure of the SLG and H. Inset: Detail of bandstructure near the K -point.

positioned over and aligned to the SLG, terminated by primary and secondary amine functional groups ($-\text{NH}_2$, $-\text{CONH}_2$) as well as hydrogen at the edge sites. For the modeling of the functional GQD [18, 19], a circular shape with a radius of $\sim 5 \text{ \AA}$ was cut out of a graphene plane centered at the center of one of the hexagons. This was a 24-atomic pristine quantum dot was obtained. Subsequently, the 12 broken bonds along the QD circumference were saturated with 3 different functional groups: four $-\text{CONH}_2$, six $-\text{NH}_2$ and two H. The functional groups were placed at a C–C bond distance from the outermost quantum dot C atoms and randomly orientated in space. Such a functionalized QD was subsequently placed 3.5 \AA above a flat graphene substrate. Finally, the periodic boundary conditions were applied using a simulation box with dimensions of $38.72 \text{ \AA} \times 38.72 \text{ \AA} \times 15 \text{ \AA}$, where the first two dimensions are along axes having 120° between them. This corresponds (in-plane) to a 16×16 supercell of graphene 2-atomic unit cell, hence yielding a model containing 540 C, 22 H, 10 N and 4 O atoms. The resulting separation in-plane between the QD periodic images was thus over 25 \AA , whereas more than 10 \AA vacuum separated QD from a periodic image of the graphene substrate.

Figure 5(b) shows the total density of states (TDOS) of SLG, H and SLG in H. We find that in the H configuration only, the TDOS is showing a subtle variation with a slight increase in the DOS at several places in the energy axis. These additional states appear from the elements of the functional groups in the GQD, which are attached with the SLG through vdW interactions, and contribute to the overall DOS of the heterostructure (cf figure SI S9). Near to the Fermi level, all configurations show a Van hove singularity-like feature in the DOS, which is the feature synonymous with the Dirac point in SLG at the K -point [65]. However, the differences in TDOS become significant when we focus near the Fermi level as shown in the inset of figure 5(b). First, we observe a noticeable increase in the DOS of the heterostructure just below the Fermi level contributing from the nitrogen in the functionalized GQD (cf figure SI S9). Furthermore, a prominent shift $\sim 0.05 \text{ eV}$ of the Dirac point with respect to the Fermi level both in the TDOS of H and DOS of the isolated SLG in H sample is noticed. This clearly signifies p-doping

in SLG due to a charge transfer and interaction with the functionalized GQD in the heterostructure with a carrier density $n \sim -0.3 \times 10^{12} \text{ cm}^{-2}$ [16, 66]. Furthermore, we observe the exact shift of the Dirac point in bandstructure in the heterostructure in comparison with SLG as shown in figure 5(c). It is observed that all the eigenvalues in the bandstructure of the heterostructure are slightly higher compared to the SLG throughout the high symmetry points ($\Gamma \rightarrow M \rightarrow K \rightarrow \Gamma$) in the BZ. On a closer inspection of the bandstructure of H, a noticeable upshift at the K -point with respect to the Fermi level (inset of figure 5(c)) provides further confirmation of the p-doping in SLG through interaction with the functionalized GQD. This also suggests that there could be a possibility of bandgap opening in SLG due to a modification of the bands around the K -point in the H configuration. However, according to Klimovskikh *et al* [67], such band opening is difficult to identify in the case of p-doping in graphene when the K -point moves above the Fermi level.

In figure 6, we show a representative example of the charge density cross section of the heterostructure containing the functional groups of $-\text{NH}_2$ and $-\text{CONH}_2$ interacting with the SLG substrate. We observe that the direction of the $-\text{NH}_2$ motif from $-\text{CONH}_2$ group is pulled downwards in the direction of the SLG carbon atom. This could suggest a weak bonding between the carbon atom from SLG and the nearest hydrogen from the $-\text{CONH}_2$ and that the interaction is not purely vdW anymore due to redistribution of the charge density in the heterostructure. Such interactions can be responsible for interlayer electron sharing and charge transfer between functional groups and the SLG in the heterostructure thus resulting in the shifting of the Dirac point with respect to the Fermi level. Moreover, such weak interaction leads to the minimization of bond length between the two materials with the functional groups orienting themselves closer the SLG surface (we recall that the functional groups had random orientations in the initial configuration before structural optimization of the heterostructure). It can be implied that the functional motifs at the edge sites are more malleable (soft lattice), enabling more out-of-plane phonon vibrations and an efficient interlayer charge transfer taking place with SLG that enhance the probability of lattice distortions along those planes [68].

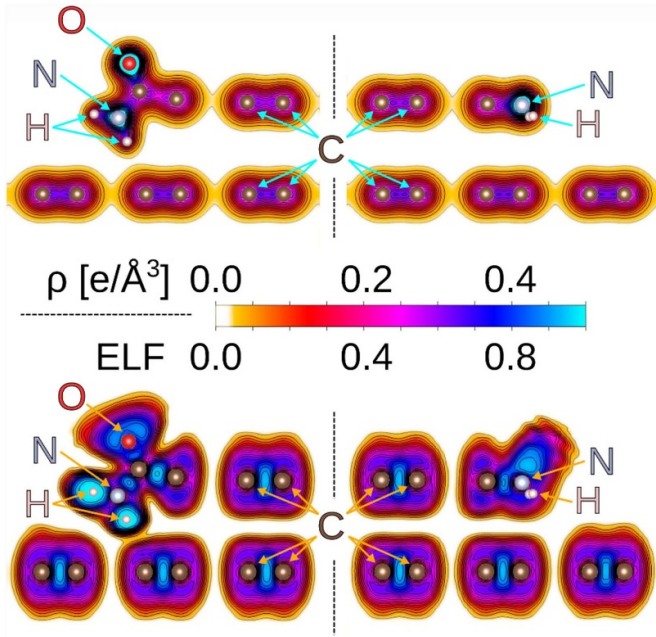


Figure 6. Simulation of charge density and electron localization function (ELF) of the heterostructure. Vertical sections of the charge density (top panel), and ELF maps (bottom panel) with the functional groups (-CONH₂, -NH₂) at the edge sites of the GQD interacting with the underneath SLG.

Furthermore, according to Cao *et al* [10] since monolayer graphene has a linear energy dispersion at its charge neutrality point, hence stacking of two graphene sheets with a slight mismatch of the lattices lead to the hybridization of their bands due to interlayer electron hopping. This results in fundamental modifications to the low-energy band structure and a superlattice modulation. We find a complementary result from the electron localization function (ELF, figure 6) of the functional motifs (-NH₂, -CONH₂) over the SLG. It is observed that especially in the vicinity of the H atoms of the -CONH₂ functional group at the edge sites of the GQD sitting on top of SLG, there is more overall spreading of the electron wavefunction due to an extended charge distribution. According to Lin *et al* [68], this type of extended charge distribution leads to soft lattice configuration seen in 1T-TaS₂ that act in favor of the lattice reconstruction and therefore CDW phase transition. Hence, it is surmised that although the electron density is more localized near the hydrogen atoms, the surrounding more electronegative atoms (O, N) especially in -CONH₂ make the electron cloud more delocalized to mainly facilitate the interlayer charge transfer possible. We attempt to ascertain the bond character due to charge transfer between the interacting materials through the closest weak C-H bonding bridge. In the map, the turquoise-colored areas correspond to highly localized electrons, while the white-yellow shaded areas indicate no electron localization. Hence, there is almost no electron localization along the interface region (C-H bridge), as the corresponding ELF is close to zero. This implies that there is no real chemical bonding at the interface between SLG and the functional GQD. However, interfacial charge transfer

occurs, possibly from a mixed hybridization (covalent-ionic) state [69]. No such effects are evident for the -NH₂ functional group, though. In summary, if we consider all the factors such as minimization of bonding length, interlayer charge transfer, spreading of the wave function around the edge functional groups and towards the interface region then we can expect to observe an increase in the EPC in the heterostructure contributed from the presence of the functionalized GQD sitting on top of SLG [68].

4. Conclusion

We encounter possible evidence of charge ordering induced phase transitions at two distinct transition temperatures ($T_1 \sim 213$ K, $T_2 \sim 325$ K) in a novel 0D–2D graphene-GQD heterostructure from the abrupt change in resistivity as a function of temperature. The stacked configuration consisting of amine functionalized GQD with SLG enabled more spreading of electron wavefunctions around the -CONH₂ functional group and efficient interlayer charge transfer. Furthermore, we considered both EEI (within the framework of weak localization and Coulomb screening) and EPC as competing interactions to establish that enhanced EPC in the heterostructure is one of the key factors for the anomalous change in resistance with possible charge ordering at high temperatures. However, direct evidence of charge density wave remains elusive at this point due to complexity of this system and remains as a future scope of research. We hope this work will motivate future research in graphene based heterogeneous 0D–2D systems to establish the link between electron phonon and electron interaction driven charge ordering through tuning of carrier densities near the Van Hove singularity in more details.

Conflict of interest

The authors declare no conflict of interest.

Supporting information

Raman Spectra from 78 to 295 K, Fitted G band and 2D band for SLG and H respectively, Magnetoresistance fitting, Details of G band phonon linewidth fitting procedure to determine electron–phonon coupling (EPC) effect (Ref: figure 2(b)), Extended Hubbard–Holstein Model, electron–electron interaction (EEI) and Coulomb screening (see figure 4), Modified Hakami–Larkin–Nagoka (HLN) and Weak Localization model, Γ_G vs ω_G dispersion relation, Characterizations of Amine-Functional Graphene Quantum Dots, *Ab initio* simulations, Optical image of the heterostructure device.






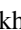


Data availability statement

Follow up work currently in progress. The data that support the findings of this study are available upon reasonable request from the authors.

Acknowledgments

R R would like to acknowledge funding by European Regional Development Fund-Project ‘MSCAfellow2@MUNI’ (No. CZ.02.2.69/0.0/0.0/18070/0009846). I J G would like to thank for the support of the Operational Program Research, Development and Education Project ‘MSCAfellow4@MUNI’ (CZ.02.2.69/0.0/0.0/20079/0017045) and the Spanish Ministry of Universities for Beatriz Galindo (BG22/000147) and Maria Zambrano funding (RSU.UDC.MZ09) transferred by the European Union Next Generation EU. We acknowledge CzechNanoLab Research Infrastructure supported by MEYS CR (LM2023051) to carry out this research. The computational results presented have been achieved using the Vienna Scientific Cluster (VSC). The authors would like to acknowledge Sumit Mandal, Vidyasagar College, Calcutta University, Subhajit Saha from the Department of Renewable energy, Maulana Abul Kalam Azad University, West Bengal, India and Jan Michalička, CEITEC Brno University of Technology, Brno 61200, Czechia for helpful discussions during this work.

ORCID iDs

Rajarshi Roy  <https://orcid.org/0000-0002-6497-6702>
 David Holec  <https://orcid.org/0000-0002-3516-1061>
 Dušan Hemzal  <https://orcid.org/0000-0002-5822-9372>
 Gundam Sandeep Kumar  <https://orcid.org/0000-0002-9339-8817>
 David Nečas  <https://orcid.org/0000-0001-7731-8453>
 Meena Dhankhar  <https://orcid.org/0000-0002-1858-0926>
 I Jénifer Gómez  <https://orcid.org/0000-0002-1493-1864>
 Lenka Zajíčková  <https://orcid.org/0000-0002-6906-8906>

References

- [1] Shimizu R, Sugawara K, Kanetani K, Iwaya K, Sato T, Takahashi T and Hitosugi T 2015 Charge-density wave in Ca-intercalated bilayer graphene induced by commensurate lattice matching *Phys. Rev. Lett.* **114** 146103
- [2] Rahnejat K, Howard C, Shuttleworth N, Schofield S, Iwaya K, Hirjibehedin C, Renner C, Aeppli G and Ellerby M 2011 Charge density waves in the graphene sheets of the superconductor CaC₆ *Nat. Commun.* **2** 558
- [3] Long G, Xu S, Zhang T, Wu Z, Wong W K, Han T, Lin J, Cai Y and Wang N 2016 Charge density wave phase transition on the surface of electrostatically doped multilayer graphene *Appl. Phys. Lett.* **109** 183107
- [4] Chang J et al 2012 Direct observation of competition between superconductivity and charge density wave order in YBa₂Cu₃O_{6.67} *Nat. Phys.* **8** 871
- [5] Pásztor A, Scarfato A, Spera M, Flicker F, Barreteau C, Giannini E, Wezel J V and Renner C 2021 Multiband charge density wave exposed in a transition metal dichalcogenide *Nat. Commun.* **12** 6037
- [6] Castro Neto A H 2001 Charge density wave, superconductivity and anomalous metallic behavior in 2D transition metal dichalcogenides *Phys. Rev. Lett.* **86** 4382
- [7] Isobe H, Yuan N F Q and Fu L 2018 Unconventional superconductivity and density waves in twisted bilayer graphene *Phys. Rev. X* **8** 041041
- [8] Yang S-L, Sobota J A, Howard C A, Pickard C J, Hashimoto M, Lu D H, Mo S-K, Kirchmann P S and Shen Z-X 2014 Superconducting graphene sheets in CaC₆ enabled by phonon-mediated interband interactions *Nat. Commun.* **5** 3493
- [9] Profeta G, Calandra M and Mauri F 2012 Phonon-mediated superconductivity in graphene by lithium deposition *Nat. Phys.* **8** 131
- [10] Cao Y, Fatemi V, Fang S, Watanabe K, Taniguchi T, Kaxiras E and Jarillo-Herrero P 2018 Unconventional superconductivity in magic-angle graphene superlattices *Nature* **556** 43
- [11] Yankowitz M, Ma Q, Jarillo-Herrero P and LeRoy B J 2019 van der Waals heterostructures combining graphene and hexagonal boron nitride *Nat. Rev. Phys.* **1** 112
- [12] Cui X et al 2015 Multi-terminal transport measurements of MoS₂ using a van der Waals heterostructure device platform *Nat. Nanotechnol.* **10** 534
- [13] He J, Kumar N, Bellus M Z, Chiu H-Y, He D, Wang Y and Zhao H 2014 Electron transfer and coupling in graphene-tungsten disulfide van der Waals heterostructures *Nat. Commun.* **5** 5622
- [14] Raja A et al 2016 Energy transfer from quantum dots to graphene and MoS₂: the role of absorption and screening in two-dimensional materials *Nano Lett.* **16** 2328
- [15] Roy R et al 2018 Resonant energy transfer in a van der Waals stacked MoS₂ - functionalized graphene quantum dot composite with ab initio validation *Nanoscale* **10** 16822
- [16] Haider G, Roy P, Chiang C-W, Tan W-C, Liou Y-R, Chang H-T, Liang C-T, Shih W-H and Chen Y-F 2016 Electrical-polarization-induced ultrahigh responsivity photodetectors based on graphene and graphene quantum dots *Adv. Funct. Mater.* **26** 620
- [17] Trentino A, Madsen J, Mittelberger A, Mangler C, Susi T, Mustonen K and Kotakoski J 2021 Atomic-level structural engineering of graphene on a mesoscopic scale *Nano Lett.* **21** 5179
- [18] Tetsuka H, Asahi R, Nagoya A, Okamoto K, Tajima I, Ohta R and Okamoto A 2012 Optically tunable amino-functionalized graphene quantum dots *Adv. Mater.* **24** 5333
- [19] Sandeep Kumar G, Roy R, Sen D, Ghorai U K, Thapa R, Mazumder N, Saha S and Chattopadhyay K K 2014 Amino-functionalized graphene quantum dots: origin of tunable heterogeneous photoluminescence *Nanoscale* **6** 3384
- [20] Nečas D and Klapetek P 2012 Gwyddion: an open-source software for SPM data analysis *Open Phys.* **10** 181–188
- [21] Froehlicher G, Lorchat E and Berciaud S 2018 Charge versus energy transfer in atomically thin graphene-transition metal dichalcogenide van der Waals heterostructures *Phys. Rev. X* **8** 011007
- [22] Kresse G and Furthmüller J 1996 Efficient iterative schemes for ab initio total-energy calculations using a plane-wave basis set *Phys. Rev. B* **54** 11169
- [23] Kresse G and Furthmüller J 1996 Efficiency of ab-initio total energy calculations for metals and semiconductors using a plane-wave basis set *Comput. Mater. Sci.* **6** 15
- [24] Kresse G and Joubert D 1999 From ultrasoft pseudopotentials to the projector augmented-wave method *Phys. Rev. B* **59** 1758
- [25] Medeiros P V C, Tsirkin S S, Stafström S and Björk J 2015 Unfolding spinor wave functions and expectation values of general operators: introducing the unfolding-density operator *Phys. Rev. B* **91** 041116
- [26] Medeiros P V C, Stafström S and Björk J 2014 Effects of extrinsic and intrinsic perturbations on the electronic structure of graphene: retaining an effective primitive cell band structure by band unfolding *Phys. Rev. B* **89** 041407

- [27] Momma K and Izumi F 2011 VESTA3 for three-dimensional visualization of crystal, volumetric and morphology data *J. Appl. Crystallogr.* **44** 1272
- [28] Ong S P, Richards W D, Jain A, Hautier G, Kocher M, Cholia S, Gunter D, Chevrier V L, Persson K A and Ceder G 2013 Python materials genomics (pymatgen): a robust, open-source python library for materials analysis *Comput. Mater. Sci.* **68** 314
- [29] Wang H, Revia R, Wang K, Kant R J, Mu Q, Gai Z, Hong K and Zhang M 2017 Paramagnetic properties of metal-free boron-doped graphene quantum dots and their application for safe magnetic resonance imaging *Adv. Mater.* **29** 1605416
- [30] Su C et al 2019 Engineering single-atom dynamics with electron irradiation *Sci. Adv.* **5** eaav2252
- [31] Ferrari A C and Basko D M 2013 Raman spectroscopy as a versatile tool for studying the properties of graphene *Nat. Nanotechnol.* **8** 235
- [32] Calizo I, Balandin A A, Bao W, Miao F and Lau C N 2007 Temperature dependence of the Raman spectra of graphene and graphene multilayers *Nano Lett.* **7** 2645
- [33] Balandin A A, Ghosh S, Bao W, Calizo I, Teweldebrhan D, Miao F and Lau C N 2008 Superior thermal conductivity of single-layer graphene *Nano Lett.* **8** 902
- [34] Cong C and Yu T 2014 Enhanced ultra-low-frequency interlayer shear modes in folded graphene layers *Nat. Commun.* **5** 4709
- [35] Nguyen K T, Abdula D, Tsai C-L and Shim M 2011 Temperature and gate voltage dependent Raman spectra of single-layer graphene *ACS Nano* **5** 5273
- [36] Bonini N, Lazzeri M, Marzari N and Mauri F 2007 Phonon anharmonicities in graphite and graphene *Phys. Rev. Lett.* **99** 176802
- [37] Gadelha A C, Nguyen V-H, Neto E G, Santana F, Raschke M B, Lamparski M, Meunier V, Charlier J-C and Jorio A 2022 Electron-phonon coupling in a magic-angle twisted-bilayer graphene device from gate-dependent Raman spectroscopy and atomistic modeling *Nano Lett.* **22** 6069
- [38] Fromm F, Wehrfritz P, Hundhausen M and Seyller T 2013 Looking behind the scenes: Raman spectroscopy of top-gated epitaxial graphene through the substrate *New J. Phys.* **15** 113006
- [39] Gao S et al 2018 Atomic-scale strain manipulation of a charge density wave *Proc. Natl Acad. Sci. USA* **115** 6986
- [40] Hoffmann F, Siebert M, Duft A and Krstić V 2022 Fingerprints of magnetoinduced charge density waves in monolayer graphene beyond half filling *Sci. Rep.* **12** 21664
- [41] Roy R, Holec D, Kratzer M, Muenzer P, Kaushik P, Michal L, Kumar G S, Zajíčková L and Teichert C 2022 Probing the charge transfer and electron-hole asymmetry in graphene-graphene quantum dot heterostructure *Nanotechnology* **33** 325704
- [42] van Loon E G C P, Rösner M, Schönhoff G, Katsnelson M I and Wehling T O 2018 Competing Coulomb and electron-phonon interactions in NbS₂ *npj Quantum Mater.* **3** 32
- [43] Johannes M D and Mazin I I 2008 Fermi surface nesting and the origin of charge density waves in metals *Phys. Rev. B* **77** 165135
- [44] Sangeetha N S, Thamizhavel A, Tomy C V, Basu S, Awasthi A M, Rajak P, Bhattacharyya S, Ramakrishnan S and Pal D 2015 Multiple charge-density-wave transitions in single-crystalline Lu₂Ir₃Si₅ *Phys. Rev. B* **91** 205131
- [45] Chen P et al 2017 Emergence of charge density waves and a pseudogap in single-layer TiTe₂ *Nat. Commun.* **8** 516
- [46] Stojchevska L, Vaskivskiy I, Mertelj T, Kusar P, Svetin D, Brazovskii S and Mihailovic D 2014 Ultrafast switching to a stable hidden quantum state in an electronic crystal *Science* **344** 177
- [47] Tsen A W et al 2015 Structure and control of charge density waves in two-dimensional 1T-TaS₂ *Proc. Natl Acad. Sci.* **112** 15054
- [48] Ma X et al 2019 Charge density wave phase transitions in large-scale few-layer 1T-VTe₂ grown by molecular beam epitaxy *ACS Appl. Mater. Interfaces* **11** 10729
- [49] Zong A et al 2018 Ultrafast manipulation of mirror domain walls in a charge density wave *Sci. Adv.* **4** eaau5501
- [50] Sipos B, Kusmartseva A F, Akrap A, Berger H, Forró L and Tutiš E 2008 From Mott state to superconductivity in 1T-TaS₂ *Nat. Mater.* **7** 960
- [51] Geremew A K, Romyantsev S, Kargar F, Debnath B, Nosek A, Bloodgood M A, Bockrath M, Salguero T T, Lake R K and Balandin A A 2019 Bias-voltage driven switching of the charge-density-wave and normal metallic phases in 1T-TaS₂ thin-film devices *ACS Nano* **13** 7231
- [52] Chen Y et al 2020 Visualizing the anomalous charge density wave states in graphene/NbSe₂ heterostructures *Adv. Mater.* **32** 2003746
- [53] Yaguchi H and Singleton J 2009 A high-magnetic-field-induced density-wave state in graphite *J. Phys.: Condens. Matter* **21** 344207
- [54] Ke F, Chen Y, Yin K, Yan J, Zhang H, Liu Z, Tse J S, Wu J, Kwang Mao H and Chen B 2019 Large bandgap of pressurized trilayer graphene *Proc. Natl Acad. Sci.* **116** 9186
- [55] Zhu X, Cao Y, Zhang J, Plummer E W and Guo J 2015 Classification of charge density waves based on their nature *Proc. Natl Acad. Sci.* **112** 2367
- [56] Li Y, Parsons C, Ramakrishna S K, Dwivedi A P, Schofield M A, Reyes A P and Guptasarma P 2020 A charge density wave-like transition in high temperature quenched Bi₂Se₃ (arXiv:10.48550/ARXIV.2002.12546)
- [57] Li Z, Zhang J, Zhou M, Zeng Y, Qi D and Li J 2020 Weak localization in 1T-TiSe₂ microflakes *Phys. Rev. B* **101** 155111
- [58] Gauzzi A et al 2014 Possible phase separation and weak localization in the absence of a charge-density wave in single-phase 1T-VS₂ *Phys. Rev. B* **89** 235125
- [59] Vaskivskiy I, Gospodaric J, Brazovskii S, Svetin D, Sutar P, Goresnik E, Mihailovic I A, Mertelj T and Mihailovic D 2015 Controlling the metal-to-insulator relaxation of the metastable hidden quantum state in 1T-TaS₂ *Sci. Adv.* **1** e1500168
- [60] Zheng G, Wang N, Yang J, Wang W, Du H, Ning W, Yang Z, Lu H-Z, Zhang Y and Tian M 2016 Weak localization effect in topological insulator micro flakes grown on insulating ferrimagnet BaFe₂O₁₉ *Sci. Rep.* **6** 21334
- [61] Mallick D, Mandal S, Ganesan R and Anil Kumar P S 2021 Existence of electron-hole charge puddles and the observation of strong universal conductance fluctuations in a 3D topological insulator *Appl. Phys. Lett.* **119** 013105
- [62] Xie Z, Wei X, Cao S, Zhang Y, Yan S, Gu G D, Li Q and Chen J-H 2021 Electron-electron interactions and weak antilocalization in few-layer ZrTe₅ devices *Phys. Rev. B* **103** 155408
- [63] Lee P A and Ramakrishnan T V 1985 Disordered electronic systems *Rev. Mod. Phys.* **57** 287
- [64] Li C, Boubeche M, Zeng L, Ji Y, Li Q, Guo D, Zhu Q, Zhong D, Luo H and Wang H 2022 Electron-electron interaction and weak antilocalization effect in a transition metal dichalcogenide superconductor *Phys. Status Solidi* **16** 2100650
- [65] Brihuega I, Mallet P, González-Herrero H, Trambly de Laissardière G, Ugeda M M, Magaud L, Gómez-Rodríguez J M, Ynduráin F and Veuille J-Y 2012

- Publisher's note: Unraveling the intrinsic and robust nature of van Hove singularities in twisted bilayer graphene by scanning tunneling microscopy and theoretical analysis [phys. rev. lett. 109, 196802 (2012)] *Phys. Rev. Lett.* **109** 209905
- [66] Froehlicher G and Berciaud S 2015 Raman spectroscopy of electrochemically gated graphene transistors: geometrical capacitance, electron-phonon, electron-electron and electron-defect scattering *Phys. Rev. B* **91** 205413
- [67] Klimovskikh I I, Otrokov M M, Voroshnin V Y, Sostina D, Petaccia L, Di Santo G, Thakur S, Chulkov E V and Shikin A M 2017 Spin-orbit coupling induced gap in graphene on Pt(111) with intercalated Pb monolayer *ACS Nano* **11** 368
- [68] Lin D *et al* 2020 Patterns and driving forces of dimensionality-dependent charge density waves in 2H-type transition metal dichalcogenides *Nat. Commun.* **11** 2406
- [69] Zheng K, Yang Q, Tan C J, Ye H Y and Chen X P 2017 A two-dimensional van der Waals CdS/germanene heterojunction with promising electronic and optoelectronic properties: DFT + NEGF investigations *Phys. Chem. Chem. Phys.* **19** 18330